Research Square

Preprints are preliminary reports that have not undergone peer review.
They should not be considered conclusive, used to inform clinical practice,
or referenced by the media as validated information.

Flexible Solar Interfacial Evaporator with Synergistic Photothermal Conversion and Phase-Change Energy Storage for Sustained Dark-State Evaporation

Yurong Yang
Zhejiang Sci-Tech University
Jinrui Xue
Zhejiang Sci-Tech University
Ruofei Zhu
Xinjiang University
Yuxin Zhu
Zhejiang Sci-Tech University
Shimin Zhai
zsm0216160163.com

Zhejiang Sci-Tech University
ChengCheng Wang
Zhejiang Sci-Tech University

Research Article

Keywords: Solar-driven interfacial evaporation, Desalination, Photothermal conversion, Phase-change energy storage, Dark-state evaporation, Continuous water production

Posted Date: November 27th, 2026

DOI: https://doi.org/10.21203/rs.3.rs-11701909/v1

License: This work is licensed under a Creative Commons Attribution 4.0 International License.
Read Full License

Additional Declarations: No competing interests reported.

Flexible Solar Interfacial Evaporator with Synergistic Photothermal Conversion and Phase-Change Energy Storage for Sustained Dark-State Evaporation

Yurong Yang [a], Jinrui Xue [a], Ruofei Zhu [b], Yuxin Zhu [a], Shimin Zhai [a]*, ChengCheng Wang [a,c]**

[a] Key Laboratory of Advanced Textile Materials and Manufacturing Technology, Zhejiang Sci-Tech University, Ministry of Education, Hangzhou, Zhejiang, 310018, PR China

[b] School of Textile and Clothing, Xinjiang Key Laboratory of Intelligent and Green Textile, Xinjiang University, Urumqi, 830017, China

[c] Key Lab of Sustainable Low-carbon Technologies for Textile Dyeing and Finishing, Ministry of Education, College of Textile Science and Engineering, Jiangnan University, Wuxi, 214122, China

Corresponding Author

* E-mail: zsm021616@163.com. (Shimin Zhai)

** E-mail: chengcwang@jiangnan.edu.cn. (ChengCheng Wang)

Abstract

Freshwater scarcity has become a global challenge, driving the development of sustainable technologies for seawater desalination and water treatment. Solar-driven interfacial evaporation provides an environmentally friendly approach by directly utilizing renewable solar energy, but its practical application is limited by intermittent solar irradiation and the resulting interruption of water production. Herein, a flexible thermal energy storage-assisted evaporator composed of biochar, CuS and polyethylene glycol (PEG) was fabricated by integrating efficient solar harvesting, interfacial photothermal conversion, and latent heat storage. For the evaporator, the porous structure of biochar (BC) promotes broadband light absorption and continuous water transport, while the photothermal component (CuS) enables efficient solar-to-thermal conversion. Meanwhile, the phase-change material (PEG) stores thermal energy during illumination and gradually releases it after the light source is removed, thereby sustaining evaporation in the dark. Under 1 kW m^{-2} irradiation, the optimized evaporator achieved an evaporation rate of 1.66 kg m^{-2} h^{-1}. After the light source was turned off, it still maintained dark-state evaporation for 1 h at an average rate of 0.53 kg m^{-2} h^{-1}. This delayed heat release effectively mitigates the interruption of water production caused by intermittent solar irradiation, providing a feasible strategy for continuous solar-driven water production under variable illumination.

Keywords: Solar-driven interfacial evaporation; Desalination; Photothermal conversion; Phase-change energy storage; Dark-state evaporation; Continuous water production

1. Introduction

Freshwater scarcity poses a critical challenge to sustainable development, fuelling rising demand for efficient and environmentally sustainable water treatment technologies[1, 2]. Although conventional desalination technologies, such as reverse osmosis and thermal distillation, have been widely applied, their energy consumption, operational costs, and infrastructure requirements remain considerable[3, 4]. Solar-driven interfacial evaporation provides an attractive alternative by localizing solar-to-thermal conversion at the air–water interface, thereby reducing heat loss to bulk water[5-8]. Owing to its direct utilization of renewable solar energy, this technology has shown considerable potential for seawater desalination and water purification[9-11].

Efficient solar interfacial evaporation requires favourable capability in light harvesting. To enhance solar energy harvesting, substantial research efforts have been devoted to developing broadband photothermal absorbers, including carbon-based materials[12-15], plasmonic materials[16-19], semiconductors[20, 21], and their composites. Thereinto, carbonaceous materials such as biochar, graphene, and carbon nanotubes are particularly attractive because of their broad spectral absorption, porous structures, and low cost[22-26]. For example, complementary coupling between carbonized cellulose and near-infrared-absorbing antimony-doped tin oxide enabled a solar absorptance of approximately 98.6% and an evaporation rate of 1.44 kg m^{-2} h^{-1} under one-sun irradiation.[27] Semiconductor photothermal materials generally enable extension of light absorption to the near-infrared region. Studies have reported that the copper-based semiconductor absorbers with strong visible-to-near-infrared responses demonstrated efficient photothermal conversion and solar evaporation.[28] However, conventional evaporators primarily depend on instantaneous solar input. Consequently, the evaporation performance declines rapidly under weak or absent illumination, which hinders continuous water production[29]. In addition to light utilization, the intermittency of

solar irradiation represents another fundamental limitation for practical solar evaporation[30].

To overcome this limitation, phase-change materials (PCMs) have been introduced into solar evaporation systems to store excess thermal energy as latent heat under illumination, and release it when solar input diminishes or vanishes[29, 31]. Studies have demonstrated that PCM-integrated interfacial evaporators can maintain an evaporation rate of approximately 0.70 kg m^{-2} h^{-1} under dark conditions by utilizing stored latent heat.[32] More recently, porous carbon frameworks have been employed to confine polyethylene glycol (PEG), enabling simultaneous solar absorption and thermal energy storage for prolonged steam generation[33]. Phase-change-assisted evaporators have also been reported to substantially boost dark-state evaporation by regulating heat storage and release during light–dark cycles.[34] Nevertheless, the direct incorporation of PCMs often suffers from leakage during phase transition, relatively low thermal conductivity, and insufficient integration between light harvesting, water transport, and thermal storage functions.[35, 36] Therefore, beyond improving photothermal conversion under illumination, combining efficient solar harvesting with thermal energy storage and delayed heat release provides a promising route for enhancing solar energy utilization and sustaining evaporation under intermittent irradiation[34, 37, 38].

Herein, a flexible solar evaporator assisted by thermal energy storage was fabricated by integrating cotton fabric (CF), copper sulfide (CuS), porous biochar (BC) and polyethylene glycol (PEG). The hydrophilic cotton fabric provides flexible support and continuous water transport, while CuS serves as the photothermal component for solar-thermal conversion. Porous biochar enhances broadband light harvesting and provides confined spaces for PEG loading, and PEG stores thermal energy as latent heat during illumination and releases it after the removal of light. Through this functional integration, a coupled process of "solar harvesting–photothermal conversion–thermal

energy storage–delayed heat release" was established to sustain evaporation beyond the illumination period. The structural characteristics, photothermal response, solar evaporation performance, dark-state evaporation, and water treatment capability of the resulting evaporators were systematically investigated. This work provides a feasible strategy for improving solar energy utilization and mitigating the interruption of water production caused by intermittent solar irradiation.

2.Experiments

2.1 Preparation of Evaporators

2.1.1 Materials and chemicals

Cotton fabric with an areal density of 118 g m^{-2} was purchased from Hongda Weaving Factory, and bamboo powder (120 mesh) was obtained from Anhui Zhumeng Bamboo Industry Co., Ltd. Sodium hydroxide (NaOH, ≥98%), dopamine hydrochloride ($C_8H_{11}NO_2$·HCl, ≥98%), tris(hydroxymethyl)aminomethane (Tris, ≥99%), copper(II) chloride dihydrate ($CuCl_2·2H_2O$, ≥98%), sodium sulfide nonahydrate ($Na_2S·9H_2O$, ≥98%), and ethyl acetate ($C_4H_8O_2$, ≥98.5%) were purchased from Shanghai Aladdin Biochemical Technology Co., Ltd. Acrylic acid was supplied by Guangzhou Wanhua New Materials Technology Co., Ltd. Potassium hydroxide (KOH), polyethylene glycol (PEG, M_n=10000), absolute ethanol, methyl orange (MO), and Reactive Red 21 were used as analytical-grade reagents. Deionized water was used throughout all experiments, and all chemicals were used as received without further purification.

2.2 Preparation of Evaporators

2.2.1 Preparation of CuS@CF

Cotton fabric was cut into 3×3 cm^2 pieces and mercerized in 30 wt% NaOH solution at room temperature for 30 min. After neutralization with 1 vol% acetic acid and washing with deionized

water until the rinsate reached approximately pH 7, the fabric was dried at 60 °C. for 12 h and denoted as CF. For polydopamine modification, 0.2 g of dopamine hydrochloride was dissolved in 100 mL of deionized water, and the pH was adjusted to 8.5 using 1 mol L^{-1} Tris solution. CF was immersed in the solution and treated at 25 ℃ and 200 rpm for 24 h. After washing and drying, the resulting fabric was denoted as PDA@CF.

CuS@CF was prepared by Cu^{2+} adsorption followed by in situ sulfidation. PDA@CF was completely immersed in 12 mM $CuCl_2$ solution at room temperature for 1 h and subsequently transferred into sufficient 12 mM Na_2S solution to ensure complete immersion for another 1 h. The resulting fabric was washed with deionized water and ethanol and dried at 60 ℃ for 12 h to obtain CuS@CF.

2.2.2 Preparation of BC@CuS Composites

Porous biochar was prepared from bamboo powder by KOH-assisted carbonization. Dried bamboo powder (120 g) was impregnated with 600 mL of 10 wt% KOH solution and dried at 60 ℃ for 12 h. The precursor was carbonized under oxygen-limited conditions at 300, 500, or 700 ℃ for 2 h at a heating rate of 3℃·min^{-1}. After grinding and sieving through a 400-mesh sieve, the products were denoted as BC_{300}, BC_{500}, and BC_{700}, respectively.

For CuS loading, 5 g of each biochar was dispersed in 150 mL of deionized water and ultrasonicated for 30 min. After the addition of 12 mM $CuCl_2$ solution and stirring for 30 min, 12 mM Na_2S solution was added dropwise. The mixture was hydrothermally treated at 70 °C for 2 h in a Teflon-lined autoclave. The products were collected, washed, and dried at 60 °C for 12 h to obtain BC_{300}@CuS, BC_{500}@CuS, and BC_{700}@CuS.

2.2.3 Preparation of BC_{500}@CuS/PEG Composites

BC_{500}@CuS/PEG composites were prepared by vacuum impregnation. PEG (3, 6, or 12 g) was melted at 90 ℃ and mixed with 2 g of BC_{500}@CuS for 10 min. The mixtures were vacuum-impregnated at 90 °C for 24 h and subsequently heated on filter paper at 90 °C to remove excess PEG. The resulting composites were denoted as BC_{500}@CuS/PEG-3, BC_{500}@CuS/PEG-6, and BC_{500}@CuS/PEG-12, respectively.

2.2.4 Fabrication of Biochar-Based Evaporators

For each evaporator, 0.1 g of the corresponding composite powder was dispersed in 5 mL of ethyl acetate and stirred for 30 min. Subsequently, 3 g of acrylic resin binder and absolute ethanol at a resin-to-ethanol mass ratio of 1 : 3 were added and stirred for 1 h. The resulting suspension was uniformly sprayed onto a 3 × 3 cm^2 cotton-fabric substrate and dried at room temperature for 1 h. Identical powder dosages and coating conditions were used for all samples.

The fabrication routes of CuS@CF and the BC_{500}@CuS/PEG-based evaporator are illustrated in **Fig. 1.**

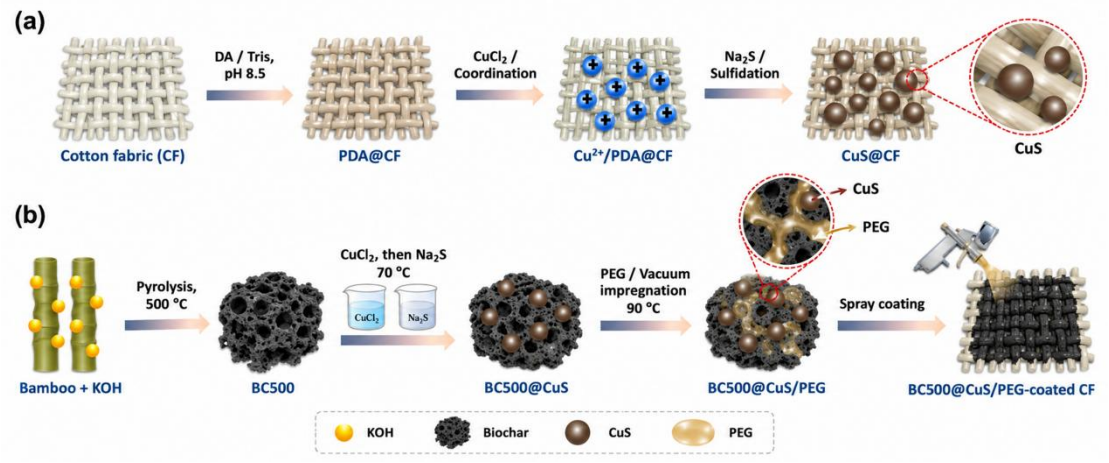


Figure. 1. Schematic illustration of the fabrication processes: (a) preparation of CuS@CF through PDA modification and in situ growth of CuS; (b) preparation of BC_{500}@CuS/PEG and subsequent fabrication of the BC_{500}@CuS/PEG-coated CF evaporator by spray coating.

As illustrated in **Fig. 1(a)**, CuS@CF was prepared through PDA modification of cotton fabric, followed by Cu^{2+} coordination and sulfidation. The catechol and amine groups introduced by PDA facilitated the in situ formation of CuS on the fibers. For the biochar-based composite evaporator, as shown in **Fig. 1(b)**, bamboo powder was subjected to KOH impregnation and pyrolysis to obtain porous biochar (BC_{500}), onto which CuS was subsequently loaded through Cu^{2+} adsorption and reaction with Na_2S. PEG was then incorporated into BC_{500}@CuS by vacuum-assisted melt impregnation, and the resulting BC_{500}@CuS/PEG composite was spray-coated onto cotton fabric to construct the evaporator. This design integrates water transport through cotton fabric, solar absorption and photothermal conversion by BC_{500}@CuS, and latent heat storage and release by PEG to support evaporation after illumination ceases.

2.3 Evaporation and Water Treatment Tests

The photothermal response of the samples was evaluated under xenon-lamp irradiation. The samples were placed on thermally insulating foam, and the irradiation intensity was adjusted to 1 kW m^{-2} (1 sun) by varying the vertical distance between the light source and the sample stage and calibrating it using a solar power meter. The surface temperatures were monitored using a handheld infrared thermal-imaging camera.

Solar-driven evaporation experiments were conducted using a self-designed evaporation setup. A xenon lamp was used to simulate solar irradiation, and the irradiation intensity was monitored using a solar power meter. The water mass change during evaporation was continuously recorded using an analytical balance. The photothermal conversion efficiency (η_{pt}) was calculated and the method was listed in the Supplementary information **(S.I. 1.1)**.

Natural seawater collected near Qingdao, China (approximately 119 °E, 36 °N), was used as

the feedwater for desalination tests. The generated vapor was condensed and collected, and the concentrations of K^+, Ca^{2+}, Na^+, and Mg^{2+} in the feedwater and condensate were measured by inductively coupled plasma optical emission spectrometry (ICP-OES; Agilent 5110, Agilent Technologies, USA). For water-treatment evaluation, the UV–vis absorption spectra of the feed solutions and corresponding condensates were measured using a UV–vis spectrophotometer (UV-2600, Shimadzu, Japan).

2.4 Characterizations

The morphologies and elemental distributions of the samples were characterized by field-emission scanning electron microscopy (FESEM; GeminiSEM 500, Carl Zeiss, Germany) coupled with energy-dispersive X-ray spectroscopy (EDS; Oxford INCA X-Act), while the microstructures of the powder samples were further examined by transmission electron microscopy (TEM; JEM-1400Flash, JEOL, Japan). The crystalline structures and chemical states were analyzed by X-ray diffraction (XRD; D8 Advance, Bruker, Germany) using Cu Kα radiation over a 2θ range of 5-90 ° at 5 ° min^{-1} and X-ray photoelectron spectroscopy (XPS; ESCALAB Xi+, Thermo Fisher Scientific, USA), respectively. Fourier-transform infrared spectroscopy (FTIR; Nicolet, Thermo Fisher Scientific, USA) was performed over 500–4000 cm^{-1} to identify the functional groups. The pore characteristics were evaluated by N_2 adsorption–desorption measurements (ASAP 2020 Plus, Micromeritics) after vacuum degassing at 120 ℃ for 10 h. Water contact angles were measured using a contact-angle analyzer (DSA25, KRÜSS, Germany) with a 5 μL water droplet, and the average of three measurements was reported. The optical properties of the samples were characterized using a UV–vis–NIR spectrophotometer (UH4150, Hitachi High-Tech, Japan) equipped with an integrating sphere over 250–2500 nm. The solar-weighted absorptance ($\overline{A}_{solar}$) was calculated based on the AM 1.5G solar spectrum, and the detailed calculation method is

provided in the Supplementary Information **(S.I. 1.2)**.

The phase-change properties of the BC@CuS/PEG composites were characterized by differential scanning calorimetry (DSC) over 25–100 °C at a heating/cooling rate of 10 °C min^{-1}. The melting and crystallization temperatures (T_m) and (T_c) and corresponding enthalpies (ΔH_m) and (ΔH_c) were obtained from the DSC curves. The PEG loading content (R_L) was calculated as:

$$R_L = \frac{\Delta H_{m,composite}}{\Delta H_{m,PEG}} \times 100\%$$

where $\Delta H_{m,composite}$ and $\Delta H_{m,PEG}$ are the melting enthalpies of the composite and pure PEG, respectively.

The thermal stability of the samples was evaluated by thermogravimetric analysis (TGA) under N_2 from room temperature to 800 °C at a heating rate of 10 °C min^{-1}.

3. Results and discussion

3.1 Structural and Compositional Characterization

The SEM images of CF, PDA@CF, and CuS@CF were shown as **Fig.2 (a)**. In **Fig. 2(a).** the pristine cotton fibers exhibited relatively smooth surfaces with well-defined contours. After PDA modification and CuS growth, the fiber surfaces became markedly rougher and were covered with particulate deposits. The EDS elemental mapping further showed relatively uniform distributions of Cu and S across the fabric surface, which may indicate the successful CuS loading. The well-dispersed CuS-containing coating on the cotton fibers can provide a photothermally active interface for subsequent solar evaporation[39].

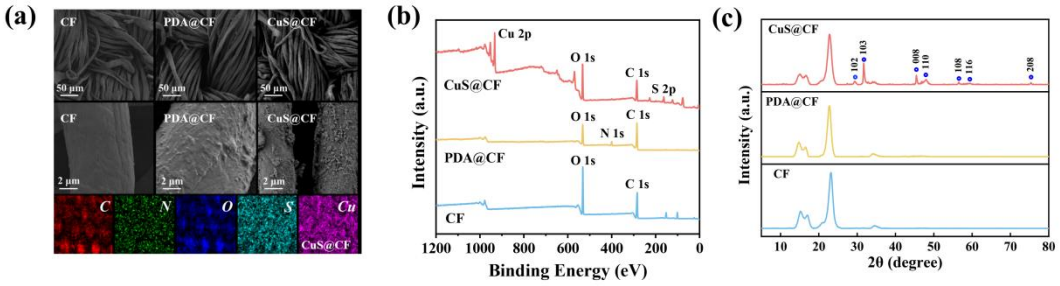


Figure 2. (a) SEM images of CF, PDA@CF, and CuS@CF, with EDS mapping of CuS@CF; (b) XPS spectra of CF, PDA@CF, and CuS@CF; (c) XRD patterns of CF, PDA@CF, and CuS@CF

The chemical composition and crystalline structure of CF, PDA@CF and CuS@CF were further analyzed. As shown in **Fig. 2(b)**, the XPS survey spectrum of CuS@CF exhibited distinct Cu 2p and S 2p signals compared with CF and PDA@CF, confirming the incorporation of Cu and S onto the cotton fabric. The high-resolution S 2p spectrum showed peaks at 162.3 and 163.6 eV respectively, which were consistent with sulfur species associated with CuS (Supplementary Information). In addition, the XRD pattern of CuS@CF in **Fig. 2(c)** displayed new diffraction peaks assignable to hexagonal covellite CuS. Based on above analysis, the CuS@CF with successful formation and relatively uniform distribution of CuS on the cotton fibers was prepared.

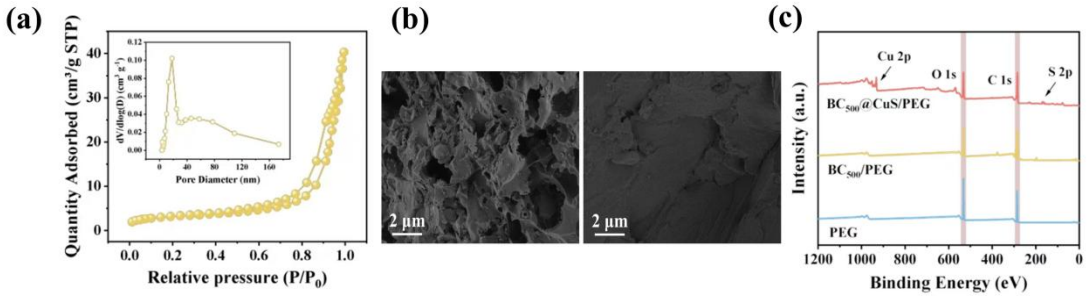


Figure 3. (a) Adsorption–desorption isotherm and pore-size distribution of BC_{500}@CuS; (b) SEM images of BC_{500}@CuS (b1) and BC_{500}@CuS/PEG (b2); (c) XPS spectra of PEG, BC_{500}/PEG, and BC_{500}@CuS/PEG

The N_2 adsorption-desorption isotherm and pore-size distribution of porous biochar

(BC_{500}@CuS) that introduced as a supporting framework for CuS was shown as **Fig.3 (a)**. In **Fig. 3(a)**, the adsorption-desorption curve was the H4 type hysteresis loops that belonged to the type IV isotherm as per the IUPAC classification[40]. The sharp increase of the curve at low relative pressure (< 0.05 P/P0) indicates the existence of micropores. Moreover, the adsorption-desorption hysteresis loops (0.5-1.0 P/P0) state the presence of mesopores and macropores without pore-blocking effect during desorption. The micropores, mesopores and macropores of BC_{500}@CuS can provide accessible space for subsequent PEG incorporation. The BET specific surface area, total pore volume, and average pore diameter of BC_{500}@CuS were 11.34 m^2g^{-1}, 0.06 cm^3g^{-1}, and 26.85 nm, respectively **(Table S1)**. The SEM images of BC_{500}@CuS and BC_{500}@CuS/PEG were shown as **Fig.3 (b)**. Compared with the BC_{500}@CuS in **Fig.3 (b1)**, the porous morphology of BC_{500}@CuS/PEG (**Fig.3 (b2)**) dispeared. Moreover, no obvious separated PEG phase was observed on the surface of BC_{500}@CuS/PEG. These changes indicate that PEG was successfully incorporated into the porous framework, which may be favorable for restricting the release of PEG during phase transition[41]. The XPS analyses for PEG, BC_{500}/PEG and BC_{500}@CuS/PEG were performed. In **Fig.3 (c)**, the spectrum of BC_{500}@CuS/PEG exhibited characteristic peaks of Cu 2p and S 2p, which were absent for PEG and BC_{500}/PEG. Overall, above results demonstrate the successful integration of PEG into BC@CuS, which is beneficial to establishing the structural basis for subsequent solar absorption, photothermal conversion and thermal-energy-storage-assisted evaporation.

3.2 Optical Properties

Efficient solar absorption is essential for rapid photothermal conversion and interfacial evaporation. As shown in **Fig. 4(a)**, pristine cotton fabric (CF) exhibited relatively weak solar absorption. After PDA modification and the in situ growth of CuS, the absorption of CuS@CF was

markedly enhanced over 200–2500 nm, reaching an average absorptance of 79.73%. This result indicates that the CuS can effectively broaden the spectral absorption capability.

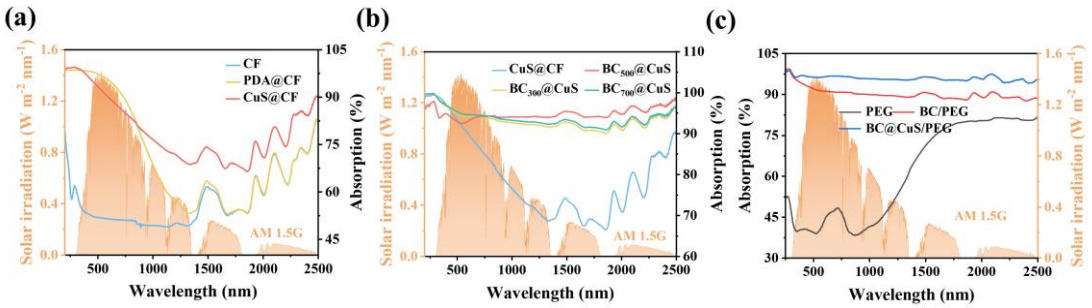


Figure 4. UV–vis–NIR absorption spectra of (a) modified cotton fabrics (CF, PDA@CF, CuS@CF); (b) CuS@CF modified with BC (BC_{300}, BC_{500}, BC_{700}); (c) PEG modified cotton fabrics (PEG, BC/PEG, BC@CuS/PEG)

The CuS@CF modified with BC and PEG modified cotton fabrics were also tested in **Fig.4 (b-c)**. In **Fig.4 (b)**, the CuS@CF modified with BC_{500} (BC_{500}@CuS) exhibited the strongest broadband absorption capability than CuS@CF, BC_{300}@CuS and BC_{700}@CuS across the UV–vis–NIR region with an average absorptance of 94.82%. Because the multiple scattering induced by the porous structure of biochar can extend the optical path length and reduce reflection losses[33]. In addition, the porous framework can provides abundant pore space for CuS loading, further contributing to broadband light harvesting[42]. In **Fig.4 (c)**, the PEG showed weak solar absorption. However, after incorporating PEG into BC_{500},, the BC_{500}@CuS/PEG retained a high average absorptance of 93.6%, which was only slightly lower than that of BC_{500}@CuS (**Fig. 4 (c)**). The result indicates that incorporating PEG into biochar can endow the composite with phase-change thermal storage functionality while maintaining high solar absorption efficiency[43].

3.3 Photothermal Properties

The photothermal conversion behaviors of the solar interfacial evaporators were evaluated by the thermal infrared imager in **Fig.5**. Under simulated solar irradiation (1 kW m^{-2}), the surface temperatures of dry CF, PDA@CF, and CuS@CF increased and reached 57.0°C, 85.2°C and 120.1 °C, respectively (**Fig.5 a,d**). Meanwhile, the surface temperature of wet CuS@CF reached 43.7 °C after 300 s of solar irradiation, which was also higher than those of CF, PDA@CF (**Fig.5 b,e**). The high surface temperature of CuS@CF further confirmed that the CuS enhanced the solar absorption and photothermal conversion capability. The lower temperature under wet conditions can be attributed to the continuous transfer of photothermal energy to the interfacial water, which is consumed during evaporation and thus reduces heat accumulation at the evaporator surface.

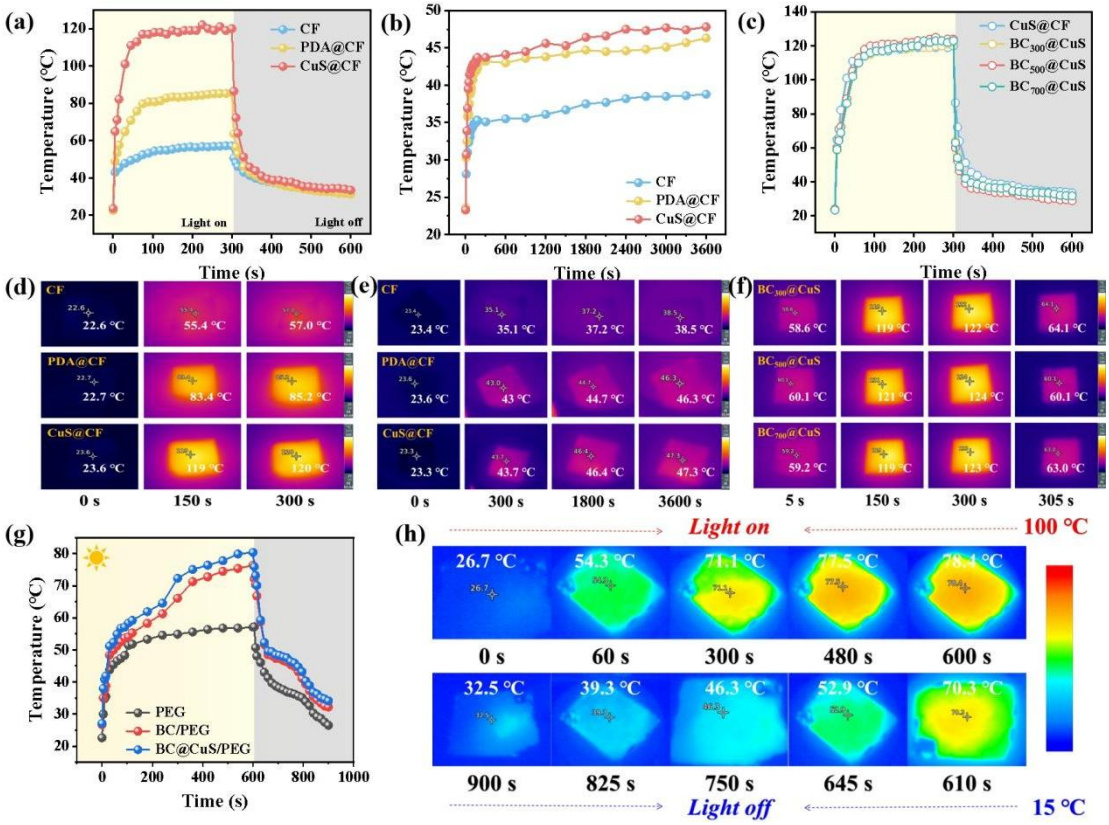


Figure 5. Temperature-time curves and infrared thermal images of (a, d) dry CF, PDA@CF and CuS@CF; (b, e) wet CF, PDA@CF and CuS@CF; (c, f) BC_{300}@CuS, BC_{500}@CuS and BC_{700}@CuS; and (g, h) PEG, BC_{500}/PEG and BC_{500}@CuS/PEG under 1 kW m^{-2} irradiation.

Moreover, the BC@CuS composites prepared with different biochars were also tested in **Fig.5 (c,f)**. The surface temperatures of BC_{300}@CuS, BC_{500}@CuS, and BC_{700}@CuS gradually approached steady state after approximately 150 s and reached approximately 122–124 °C after 300 s of irradiation. Thereinto, the BC_{500}@CuS showed the highest temperature (124 °C), indicating that the BC_{500} was favorable for light harvesting and localized heat accumulation. The result was also consistent with its high optical absorption in **Fig. 4 (b)**.

The phase-change thermal-regulation performance of BC_{500}@CuS/PEG was presented in **Fig.5 (g, h)**. In **Fig. 5(g)**, the surface temperature of BC_{500}@CuS/PEG increased rapidly from 26.7 °C to the plateau of approximately 77.5–78.4 °C after about 480 s. This plateau originates from the absorption and storage of thermal energy as latent heat during the solid–liquid phase transition of PEG[44]. After the light was switched off, the sample exhibited an average cooling rate of approximately 0.086 °C s^{-1}, showing a delayed cooling behavior (**Fig. 5(h)**). The result indicates that the latent heat stored by PEG can be gradually released during the liquid–solid phase transition, providing a basis for sustained heat supply under dark conditions.

3.4 Solar Evaporation Performance

The solar-driven evaporation performances of CF, PDA@CF, and CuS@CF were evaluated in **Fig.6 (a, d)** under the simulated solar irradiation (1.0 sun). As shown in **Fig.6 (a)**, the water mass decreased continuously with irradiation time for all samples. However, the substantial differences were observed in the rates of water loss in **Fig.6 (d)**. The pristine CF exhibited relatively low evaporation performance because of its limited solar absorption and photothermal conversion capability, whereas PDA modification led to a moderate improvement[45]. After the in situ growth of CuS, the evaporation rate increased to 1.36 kg m^{-2} h^{-1}, corresponding to a solar-to-vapor

conversion efficiency of 80.6%. This enhancement is consistent with the improved optical absorption and photothermal response of CuS@CF, demonstrating the contribution of CuS to interfacial solar evaporation[46].

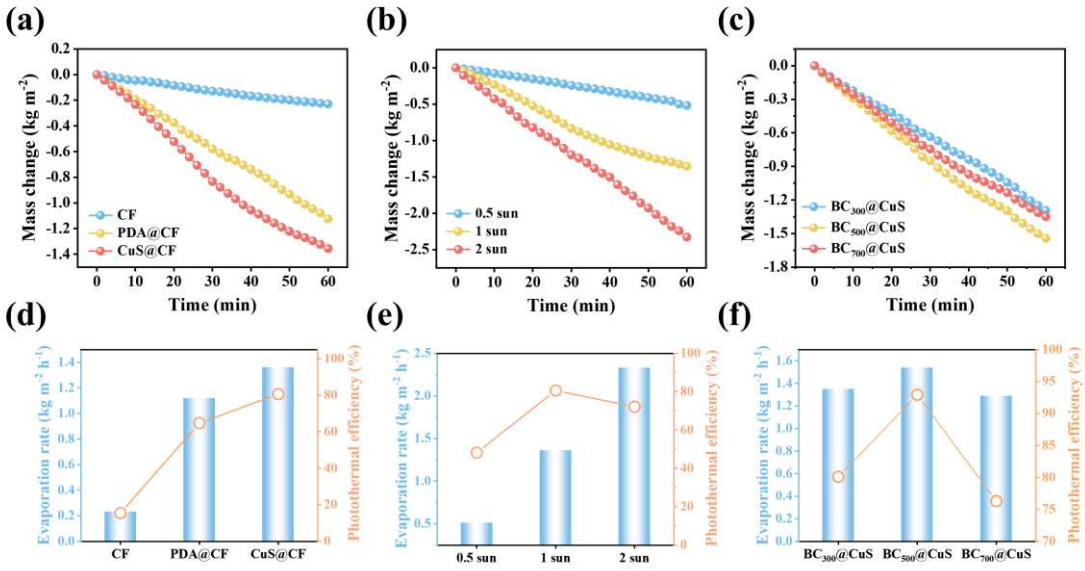


Figure 6. Solar-driven and dark-state evaporation performance. (a) Water-mass change and evaporation performances of CF, PDA@CF, and CuS@CF under 1 kW m^{-2} irradiation; (b) evaporation performance of CuS@CF under different irradiation intensities; (c) evaporation performance of BC@CuS evaporators prepared with different biochars.

The evaporation behavior of CuS@CF was further investigated under different irradiation intensities (**Fig.6 (b, e)**). The evaporation rate increased continuously with increasing solar intensity, whereas the solar-to-vapor conversion efficiency decreased at higher irradiation levels (**Fig.6 (e)**). This trend may result from increased interfacial water consumption and possible limitations in capillary water replenishment, together with enhanced conductive, convective, and radiative heat losses at elevated temperatures[47, 48]. These results indicate that evaporation performance is governed not only by photothermal conversion but also by the balance between water transport and interfacial heat utilization[49].

The evaporation performance of the BC@CuS composites prepared using biochars carbonized at different temperatures was evaluated, as shown in **Fig. 6(c)**. Among these samples, BC_{500}@CuS exhibited relatively favorable evaporation performance, indicating that biochar prepared at 500 °C was suitable for enhancing solar harvesting and interfacial evaporation. Therefore, BC_{500} was selected for subsequent optimization of CuS loading. The optimized BC_{500}@16CuS evaporator achieved an evaporation rate of 1.69 kg m^{-2} h^{-1} and a solar-to-vapor conversion efficiency of 94.05% (**Fig. Sx**). This sample is hereafter denoted as BC_{500}@CuS.

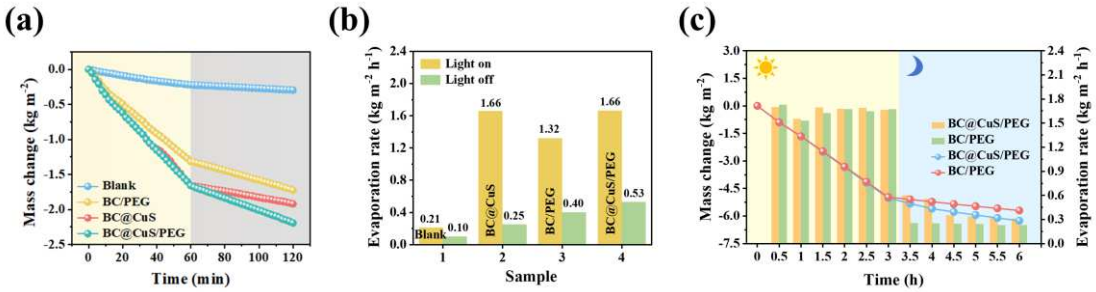


Figure 7. Solar-driven and dark-state evaporation performance. (a) Water-mass changes of the blank control, BC/PEG, BC@CuS, and BC@CuS/PEG during illumination and subsequent darkness; (b) corresponding evaporation rates under light-on and light-off conditions; (c) water-mass changes and evaporation rates of BC/PEG and BC@CuS/PEG during 3 h of illumination followed by 3 h of darkness. The irradiation intensity was 1 kW m^{-2}.

PEG was subsequently incorporated into BC_{500}@CuS to introduce phase-change thermal-energy storage. The evaporation performance was evaluated under 1 kW m^{-2} irradiation with an evaporation area of 9 cm^2, using pure water as the blank control. **Fig. 7(a)** presents the water-mass changes during 1 h of illumination followed by 1 h of darkness. As shown in **Fig. 7(b)**, both BC_{500}@CuS and BC_{500}@CuS/PEG exhibited an evaporation rate of 1.66 kg m^{-2} h^{-1} during illumination, indicating that PEG incorporation maintained the evaporation performance under the

tested conditions. In comparison, BC/PEG exhibited a lower evaporation rate of 1.32 kg m^{-2} h^{-1}.

After irradiation ceased, BC_{500}@CuS/PEG exhibited an average evaporation rate of 0.53 kg m^{-2} h^{-1}, compared with 0.25 kg m^{-2} h^{-1} for BC_{500}@CuS (**Fig. 7(b)**). Consequently, its cumulative evaporation during the 1 h dark period exceeded that of BC_{500}@CuS by 0.28 kg m^{-2}, increasing the total evaporation over the complete light-dark test. BC/PEG also maintained an average dark-state evaporation rate of 0.40 kg m^{-2} h^{-1}, higher than the 0.10 kg m^{-2} h^{-1} measured for pure water. The enhanced dark-state evaporation of the PEG-containing samples may be attributed to the gradual release of stored sensible and latent heat during cooling, particularly the latent heat released during PEG solidification[32, 50, 51].

Fig. 7(c) further compares BC/PEG and BC_{500}@CuS/PEG during 3 h of illumination followed by 3 h of darkness. Both samples continued to exhibit water-mass loss after the light source was switched off, although their evaporation rates gradually decreased. Compared with BC/PEG, BC_{500}@CuS/PEG maintained higher evaporation rates throughout the dark period and achieved greater cumulative evaporation by the end of the test. These results support the benefit of combining CuS with the PEG-containing framework to sustain evaporation after light interruption[32].

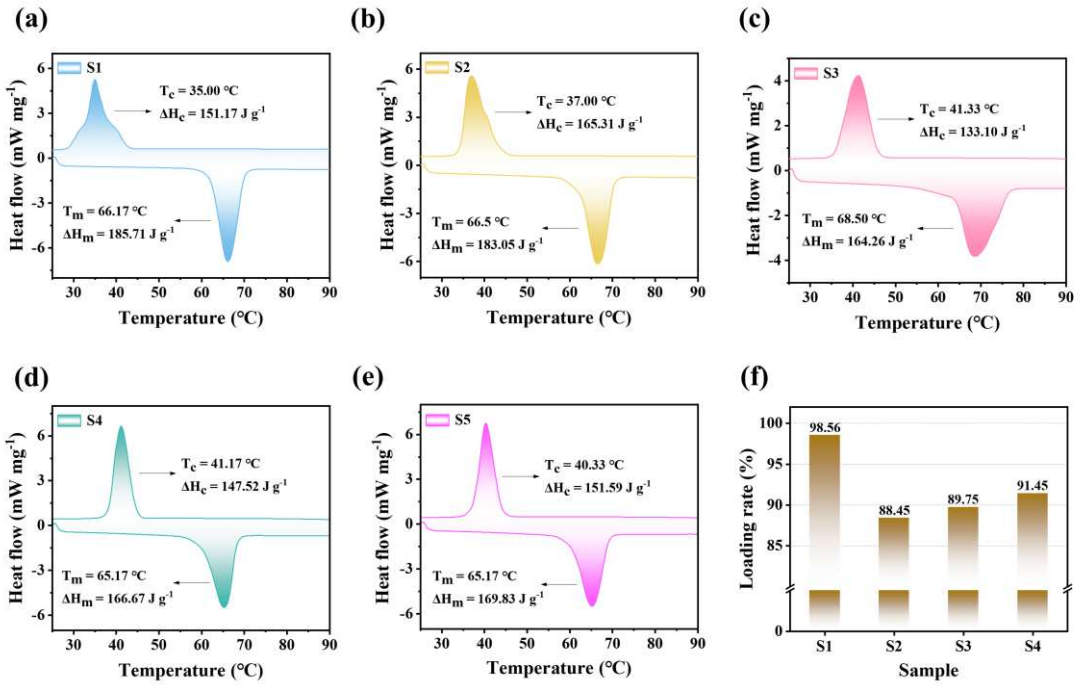


Figure 8. Phase-change energy storage properties. (a-e) DSC curves of S1-S5; (f) PEG loading ratios of S2-S5. S1 denotes pristine PEG, S2 denotes BC_{500}/PEG, and S3-S5 denote BC_{500}@CuS/PEG composites prepared with PEG feed amounts of 3, 6, and 12 g, respectively.

The phase-change properties of BC_{500}@CuS/PEG were investigated to examine its thermal-energy storage capacity. As shown in **Fig. 8(a-e)**, the samples exhibited distinct melting and crystallization peaks, with melting peak temperatures ranging from 65.17 to 68.50 °C and crystallization peak temperatures ranging from 35.00 to 41.33 °C. These endothermic and exothermic peaks correspond to heat absorption during PEG melting and heat release during crystallization, respectively.

The composites shown in **Fig. 8(c-e)** exhibited melting enthalpies of 164.26, 166.67, and 169.83 J g^{-1}, respectively. Among these three composites, the sample prepared with a PEG feed amount of 12 g exhibited the highest melting enthalpy of 169.83 J g^{-1}, together with a PEG loading rate of 91.45% (**Fig. 8(f)**). Its melting and crystallization peak temperatures were 65.17 and 40.33 °C, respectively, and its crystallization enthalpy reached 151.59 J g^{-1}. These results demonstrate

substantial latent-heat storage and release capacity, providing a thermal basis for energy storage during illumination and heat release after light interruption.

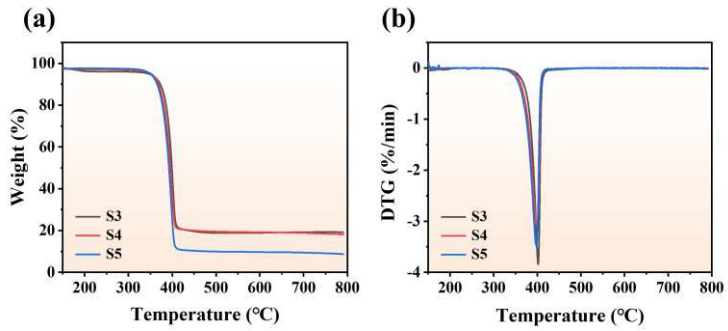


Figure 9. Thermal stability of BC_{500}@CuS/PEG composites. (a) TG curves and (b) corresponding DTG curves of S3-S5, prepared with PEG feed amounts of 3, 6, and 12 g, respectively.

The thermal stability of BC_{500}@CuS/PEG was further evaluated by TG and DTG analyses (**Fig. 9**). As shown in **Fig. 9(a)**, the composite retained a residual mass of 12.27 wt% after thermal decomposition. The corresponding DTG curve exhibited a maximum mass-loss rate at 397.6 ℃ (**Fig. 9(b)**). This decomposition peak temperature was substantially higher than the surface temperatures measured during the photothermal tests.

3.5 Water Treatment and Stability

As shown in **Fig. 10(a)**, increasing the NaCl concentration from 3.5 to 10 wt% caused only a slight decrease in the evaporation rate of BC_{500}@CuS, from 1.692 to 1.678 kg m^{-2} h^{-1}, corresponding to a reduction of 0.83%. BC_{500}@CuS also maintained an evaporation rate of approximately 1.68 kg m^{-2} h^{-1} after eight consecutive cycles in 3.5 wt% NaCl solution (**Fig. 10(b)**). These results indicate limited sensitivity to salinity within the tested range and stable performance during repeated operation. This stability may be supported by continuous water supply through the hydrophilic cotton substrate and porous biochar framework, helping maintain a wetted evaporation interface[52, 53].

The desalination performance of BC_{500}@CuS/PEG was evaluated using real seawater. As shown in **Fig. 10(c,d)**, the concentrations of K^+, Ca^{2+}, Na^+, and Mg^{2+} decreased markedly after evaporation-condensation, with rejection efficiencies exceeding 99% for all four ions. In particular, the Na^+ concentration decreased from 9496.14 to 8.207 mg L^{-1}, corresponding to a rejection efficiency of 99.91%. This separation is consistent with the retention of nonvolatile salt ions in the feed solution during water vaporization, allowing condensate with substantially reduced salt concentrations to be collected.

Dye separation was further examined using methyl orange and Reactive Red 21 solutions, each at 50 mg L^{-1}. The feed solutions exhibited characteristic absorption peaks at 460 and 530 nm, respectively (**Fig. 10(e,f)**). After treatment with BC_{500}@CuS/PEG, these peaks nearly disappeared in the condensates, which were clear and colorless. This behavior is consistent with the low volatility of the dye solutes, which limits their transfer into the vapor phase. Together with the ion-rejection results, these observations demonstrate the effectiveness of evaporation-condensation in separating the tested nonvolatile contaminants from water.

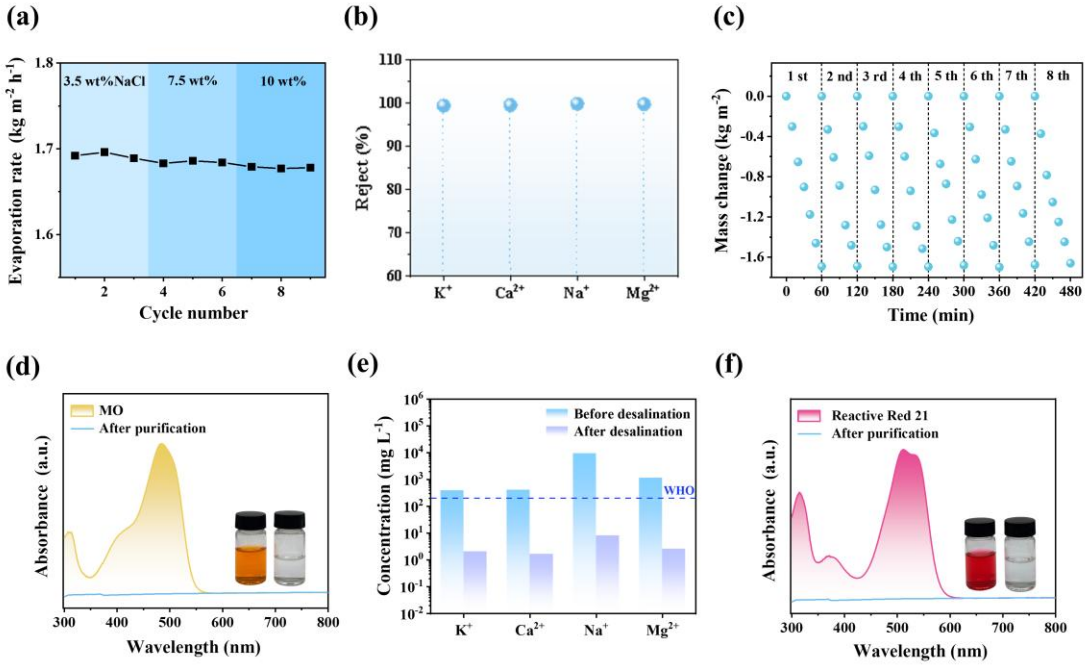


Figure 10. Water treatment performance and operational stability of the composite evaporators. (a) Evaporation rates of BC_{500}@CuS in NaCl solutions of different concentrations; (b) cycling performance of BC_{500}@CuS over eight consecutive cycles in 3.5 wt% NaCl solution; (c) major ion concentrations in feed seawater and condensate obtained using BC_{500}@CuS/PEG; (d) corresponding ion rejection efficiencies; (e, f) UV – vis absorption spectra of methyl orange and Reactive Red 21 feed solutions and their corresponding condensates, respectively.

Conclusion

A flexible composite solar interfacial evaporator integrating CuS-mediated photothermal conversion, biochar-enhanced broadband light harvesting, and PEG-based phase-change thermal-energy storage was developed using hydrophilic cotton fabric as a continuous water-transport substrate. The porous BC_{500}@CuS framework facilitated solar harvesting and interfacial heat generation, enabling the optimized evaporator to achieve an evaporation rate of 1.69 kg m^{-2} h^{-1} and a solar-to-vapor conversion efficiency of 94.05% under 1 kW m^{-2} irradiation. After PEG incorporation, BC_{500}@CuS/PEG exhibited a melting enthalpy of 169.83 J g^{-1} while maintaining a high illuminated evaporation rate of 1.66 kg m^{-2} h^{-1}. PEG stored part of the photothermally generated energy as latent heat and gradually released it after irradiation ceased. Consequently, the composite sustained dark-state evaporation for 1 h at an average rate of 0.53 kg m^{-2} h^{-1}, producing 0.28 kg m^{-2} more water than the PEG-free evaporator. The evaporator also maintained stable performance under saline and cycling conditions, achieved over 99% rejection of major seawater ions, and effectively separated methyl orange and Reactive Red 21. These results demonstrate that coupling efficient photothermal conversion with latent-heat storage provides a feasible strategy for sustained desalination and water purification under intermittent solar irradiation.

Supplementary Materials

The supporting information includes calculation methods for the evaporation rate, solar-to-vapor conversion efficiency, photothermal conversion efficiency, and solar-weighted absorptance; Table S1: Textural properties of BC_{300}@CuS, BC_{500}@CuS, and BC_{700}@CuS; Figure S1: Effect of CuS loading on the solar-driven evaporation performance of BC_{500}@CuS under 1 kW · m^{-2} irradiation.

Data Availability Statement

The raw data supporting the conclusions of this article will be made available by the authors on request.

Conflicts of Interest

The authors declare no conflict of interest. The funders did not participate in selecting the research topic, designing the study, collecting, analyzing, or interpreting the data, preparing the manuscript, or deciding to publish the results.

Acknowledgements

This research was supported by Key Research and Development Program of Xinjiang Uygur Autonomous Region [2025B04040-003], the Open Fund of the Key Laboratory of Advanced Textile Materials and Preparation Technology of the Ministry of Education [14310031202501-02-17].

References

[1] Lim H W, Park S H, Lee S J. 3d thermoresponsive hydrogel with enhanced water uptake and active evaporation for effective interfacial solar steam generation [J]. Desalination, 2023, 550.

[2] Mekonnen M M, Hoekstra A Y. Four billion people facing severe water scarcity [J]. Science Advances,

2016, 2(2).

[3] Gude V G, Nirmalakhandan N, Deng S G. Renewable and sustainable approaches for desalination [J]. Renewable & Sustainable Energy Reviews, 2010, 14(9): 2641-2654.

[4] Elimelech M, Phillip W A. The future of seawater desalination: Energy, technology, and the environment [J]. Science, 2011, 333(6043): 712-717.

[5] Ding M C, Zhao D M, Duan Z Y, et al. Bio-inspired solar evaporators for stable and efficient desalination of high-salinity brine with zero liquid discharge [J]. Science Bulletin, 2025, 70(17): 2812-2823.

[6] Xu N, Li J L, Wang Y, et al. A water lily-inspired hierarchical design for stable and efficient solar evaporation of high-salinity brine [J]. Science Advances, 2019, 5(7).

[7] Ghasemi H, Ni G, Marconnet A M, et al. Solar steam generation by heat localization [J]. Nature Communications, 2014, 5.

[8] Fang Y M, Gao H M, Cheng K T, et al. An overview of photothermal materials for solar-driven interfacial evaporation [J]. Chinese Chemical Letters, 2025, 36(3).

[9] Motora K G, Wu C M, Naseem S. Magnetic recyclable self-floating solar light-driven wo2.72/fe3o4 nanocomposites immobilized by janus membrane for photocatalysis of inorganic and organic pollutants [J]. Journal of Industrial and Engineering Chemistry, 2021, 102(25-34).

[10] Wu C M, Cheng C T, Tessema A A, et al. Staple carbon fabric/polyurethane janus membranes for photothermal conversion and interfacial steam generation [J]. Journal of Polymer Research, 2023, 30(6).

[11] Zuo S Y, Xia D S, Guan Z Y, et al. Dual-functional cuo/cn for highly efficient solar evaporation and water purification [J]. Separation and Purification Technology, 2021, 254(10).

[12] Chen S L, Sun L, Huang Y Q, et al. Biochar-based interfacial evaporation materials derived from

lignosulfonate for efficient desalination [J]. Carbon Neutralization, 2023, 2(4): 494-509.

[13] Vasudevan G, Pakkath J J, Phukan I S, et al. Experimental investigation on single slope solar still integrated pcm-bamboo biochar composites for sustainable water production [J]. Separation and Purification Technology, 2026, 404(20).

[14] Ito Y, Tanabe Y, Han J H, et al. Multifunctional porous graphene for high-efficiency steam generation by heat localization [J]. Advanced Materials, 2015, 27(29): 4302-4307.

[15] Li X Q, Xu W C, Tang M Y, et al. Graphene oxide-based efficient and scalable solar desalination under one sun with a confined 2d water path [J]. Proceedings of the National Academy of Sciences of the United States of America, 2016, 113(49): 13953-13958.

[16] Liu G H, Xu J L, Chen T, et al. Progress in thermoplasmonics for solar energy applications [J]. Physics Reports-Review Section of Physics Letters, 2022, 981(1-50).

[17] Yang H, Li D, Zheng X D, et al. High freshwater flux solar desalination via a 3d plasmonic evaporator with an efficient heat-mass evaporation interface [J]. Advanced Materials, 2023, 35(47): 10.

[18] Bae K, Kang G, Cho S K, et al. Flexible thin-film black gold membranes with ultrabroadband plasmonic nanofocusing for efficient solar vapour generation [J]. Nature Communications, 2015, 6(9).

[19] Zhou L, Tan Y L, Wang J Y, et al. 3d self-assembly of aluminium nanoparticles for plasmon-enhanced solar desalination [J]. Nature Photonics, 2016, 10(6): 393.

[20] Du C K, Zhao X P, Qian X, et al. Heat-localized solar evaporation: Transport processes and applications [J]. Nano Energy, 2023, 107(20).

[21] Liu H W, Chen C J, Wen H, et al. Narrow bandgap semiconductor decorated wood membrane for high-efficiency solar-assisted water purification [J]. Journal of Materials Chemistry A, 2018, 6(39): 18839-18846.

[22] Zeng Y, Yao J F, Horri B A, et al. Solar evaporation enhancement using floating light-absorbing magnetic particles [J]. Energy & Environmental Science, 2011, 4(10): 4074-4078.

[23] Li T, Liu H, Zhao X P, et al. Scalable and highly efficient mesoporous wood-based solar steam generation device: Localized heat, rapid water transport [J]. Advanced Functional Materials, 2018, 28(16).

[24] Xu N, Hu X Z, Xu W C, et al. Mushrooms as efficient solar steam-generation devices [J]. Advanced Materials, 2017, 29(28).

[25] Zeng L, Deng D X, Zhu L Y, et al. Biomass photothermal structures with carbonized durian for efficient solar-driven water evaporation [J]. Energy, 2023, 273(10).

[26] Dao V D, Choi H S. Carbon-based sunlight absorbers in solar-driven steam generation devices [J]. Global Challenges, 2018, 2(2): 14.

[27] Zhang W, Zheng T, Zhu H G, et al. Insight into the role of the channel in photothermal materials for solar interfacial water evaporation [J]. Renewable Energy, 2022, 193(706-714).

[28] Shridharan T S, Lee J H, Tan R F, et al. Unique photothermal material: Copper phosphate (cu3p2o8) with broadband visible-to-near-infrared absorption properties for efficient solar steam generation [J]. Desalination, 2024, 579(9).

[29] Ma H L, Chen X W, Yang T T, et al. Enabling all-weather interfacial solar evaporation: A latent heat-regulated evaporator with janus phase change microcapsules [J]. Chemical Engineering Journal, 2026, 534(13).

[30] Wang X, Jia W Y, Liu Z H, et al. Fabric-coordinated phase-change energy storage solar evaporator for all-day evaporation [J]. Desalination, 2026, 619(9).

[31] Zhou P L, Sun F, Xu L S, et al. Phase-change photothermal foam enables continuous hypersaline

brine desalination [J]. Environmental Science and Ecotechnology, 2026, 31(10).

[32] Gong B Y, Yang H C, Wu S H, et al. Phase change material enhanced sustained and energy-efficient solar-thermal water desalination [J]. Applied Energy, 2021, 301(9).

[33] Basuny B N, Kospa D A, Ibrahim A A, et al. Stable polyethylene glycol/biochar composite as a cost-effective photothermal absorber for 24 hours of steam and electricity cogeneration [J]. Rsc Advances, 2023, 13(44): 31077-31091.

[34] Lan J R, Hong W P, Dong C Y, et al. Enhancing the sustainability of interfacial evaporation to mitigate solar intermittency via phase change thermal storage [J]. Chemical Engineering Journal, 2024, 500(8).

[35] Yuan Z Q, Du C W, Qiao L L, et al. Solid-liquid phase change materials for solar-driven interfacial evaporation: Principles, design optimization, and emerging advances in sustainable seawater desalination [J]. Chemical Engineering Journal, 2025, 516(25).

[36] Chan K Y, Dong X L, Yang Y F, et al. A heterogeneous nanocomposite architecture with contrasting thermal conductivity and hydrophilicity for synergistic solar-thermal storage and evaporation [J]. Materials Horizons, 2025, 12(14): 5175-5186.

[37] Liu Y C, Zou M M, Chen W J, et al. Cds/pda enhanced solar-driven phase change evaporator for continuous seawater desalination [J]. Separation and Purification Technology, 2024, 354(10).

[38] Sun Y Q, Bao J K, Li J L, et al. Integrating a phase-change core and a photothermal fabric shell for high-efficiency solar desalination and water treatment [J]. Acs Applied Materials & Interfaces, 2026, 18(37): 50811-50820.

[39] Sun W B, Qi H, Li T, et al. Salt-resistant continuous solar evaporation composites based on nonwovens with synergistic photothermal effect of graphene oxide/copper sulphide [J]. Rsc Advances,

2024, 14(39): 28984-28997.

[40] Thommes M, Kaneko K, Neimark A V, et al. Physisorption of gases, with special reference to the evaluation of surface area and pore size distribution (iupac technical report) [J]. Pure and Applied Chemistry, 2015, 87(9-10): 1051-1069.

[41] Zhang J K, Zheng Z Y, Xu L, et al. Light- and electro-driven phase change materials derived from activated porous biochar nanosheets and encapsulated polyethylene glycol [J]. Colloids and Surfaces a-Physicochemical and Engineering Aspects, 2024, 690(10).

[42] Li S Y, Huo Y J, Yan T, et al. Sugarcane derived carbon@cus-octadecanol composite phase change materials for efficient solar thermal storage [J]. Progress in Natural Science-Materials International, 2024, 34(4): 803-813.

[43] Baniasadi H, Fathi Z, Abidnejad R, et al. Biochar-infused cellulose foams with peg-based phase change materials for enhanced thermal energy storage and photothermal performance [J]. Carbohydrate Polymers, 2025, 367(13).

[44] Kolgesiz S, Tas C E, Sisman N, et al. Flexible and inherently photothermal waterborne polydopamine/polyurethane/phase change material foams for light-to-thermal energy conversion and thermal energy storage [J]. Industrial & Engineering Chemistry Research, 2024, 63(35): 15485-15498.

[45] Xu Y S, Tang B, Fang X, et al. A facile approach to fabricate sustainable and large-scale photothermal polydopamine-coated cotton fabrics for efficient interfacial solar steam generation [J]. Industrial & Engineering Chemistry Research, 2022, 61(49): 18109-18120.

[46] Wang Z G, Zhang X F, Shu L, et al. Copper sulfide integrated functional cellulose hydrogel for efficient solar water purification [J]. Carbohydrate Polymers, 2023, 319(8).

[47] Singh S C, ElKabbash M, Li Z L, et al. Solar-trackable super-wicking black metal panel for

photothermal water sanitation [J]. Nature Sustainability, 2020, 3(11): 938.

[48] Cao Y H, Wang J M, Guan W X, et al. Spatially regulated water-heat transport by fluidic diode membrane for efficient solar-powered desalination and electricity generation [J]. Nature Communications, 2025, 16(1): 13.

[49] Wu X, Lu Y, Ren X H, et al. Interfacial solar evaporation: From fundamental research to applications [J]. Advanced Materials, 2024, 36(23): 63.

[50] Niu R, Ren J X, Koh J J, et al. Bio-inspired sandwich-structured all-day-round solar evaporator for synergistic clean water and electricity generation [J]. Advanced Energy Materials, 2023, 13(45): 10.

[51] Gu X B, Dong K J, Peng L H, et al. Round-the-clock interfacial solar vapor generator enabled by form-stable phase change materials with enhanced photothermal conversion capacity [J]. Energy Conversion and Management, 2023, 277(12).

[52] Liu Z X, Zhou Z, Wu N Y, et al. Hierarchical photothermal fabrics with low evaporation enthalpy as heliotropic evaporators for efficient, continuous, salt-free desalination [J]. Acs Nano, 2021, 15(8): 13007-13018.

[53] Yang K J, Pan T T, Dang S C, et al. Three-dimensional open architecture enabling salt-rejection solar evaporators with boosted water production efficiency [J]. Nature Communications, 2022, 13(1): 8.

Supplementary Files

This is a list of supplementary files associated with this preprint. Click to download.

- Supportinginformation.docx